CHAPTER 4

Pressure induced superconducting state in ideal topological insulator $BiSbTe_3$

Chapter 4

4.1 Introduction

Topological insulator (TI) is a new quantum state of matter which has attracted a huge attention because of their unique properties and potential technological applications [1]–[6]. While Bi_2Se_3, Bi_2Te_3 and Sb_2Te_3 are mostly studied three-dimensional TIs, very few reports are available on $BiSbTe_3$ TI compounds so far [86]–[89]. Usually, the conductivity of Bi_2Te_3 shows *n*-type behavior due to the formation of Te-vacancies and Sb_2Te_3 shows *p*-type behavior for formation of anti-site defects [4], [28], [90], [91]. The topological surface state (TSS) exists in the energy gap between bulk conduction band (BCB) and bulk valence band (BVB) and exhibits a Dirac cone like band dispersion with a crossing point, so called Dirac point (DP), at the Γ point of the surface Brillouin zone. In case of Bi_2Te_3 TI the Fermi level (E_F) lies in the BCB. On the other hand, the E_F of the Sb_2Te_3 TI lies in the BVB locating the DP above E_F. The position of the DP and E_F may be tuned simultaneously by mixing of these two compounds. This may lead to an ideal TI in which E_F and the DP coincides in the insulating bulk band gap, which paves the way to apply topological surface states for future devices. The reported stoichiometric of Bi/Sb for the transition from *n* to *p*-type in $(Bi_{1-x}Sb_x)_2Te_3$ is debatable [92]–[95].

Furthermore, recently, pressure-induced superconductivity has been observed in Bi_2Te_3, Bi_2Se_3 and Sb_2Te_3 topological insulators [96]–[98]. Majorana fermions, potentially fruitful in quantum computing can be expected at the edge states in these topological materials [99]–[101]. In this regard, $BiSbTe_3$ is a potential candidate to observe superconducting state where we have shown in the present investigation that the DP is located exactly at the Fermi energy.

In this chapter, we have found emergence of the superconducting states under pressure in $BiSbTe_3$ TI. We have revealed that the DP of TSS is exactly located at E_F and observed the hole-like bulk conductivity due to crossing of BVB to the E_F.

4.2 Experimental Details

We have grown the single crystal $BiSbTe_3$ 3D TIs by a modified Bridgman method as has been reported elsewhere [62] with the stoichiometric amount of 1:1:3 for the mixture of Bi, Sb and Te powders respectively with purity of 99.999%. The cleaved shiny silver colored single crystal was characterized by X-Ray diffraction (XRD). The magnetotransport properties and pressure dependent XRD were measured at Institute for Solid State Physics, University of Tokyo, Japan by using physical property measurement system (PPMS) with varying magnetic field up to 7 T. The X-ray photoelectron diffraction (XPD) experiment was carried out for vacuum cleaved $BiSbTe_3$ crystal at room temperature at the PEARL (X03DA) beamline [102] of the Swiss Light Source synchrotron facility using linear polarization of photons. The normal to the sample surface, the X-ray beam, the polarization vector of photons, and the axis of the analyzer lens were oriented in the horizontal plane, while the entrance slit of the Scienta EW4000 electron analyzer was oriented vertically. To probe the Dirac point and the surface states of $BiSbTe_3$, the ARPES experiment was performed by Laser-ARPES at the Hiroshima Synchrotron Radiation Center (HiSOR) using s-polarized light of 6.45 eV and measured with a hemispherical analyzer (VG Scienta SES R4000) at 20 K and 60 K [103]. The sample was cleaved in-situ at ~22 K in an ultrahigh vacuum below 8×10^{-9} Pa.

4.3 Results and Discussion

4.3.1 Experimental Study

The X-ray diffraction pattern indicates that the crystal growth direction is along the *c*-axis as shown in figure 4.1 (a) (Inset shows the Laue diffraction patterns of as-grown $BiSbTe_3$ single crystal). Weyrich *et al.* [104] estimated Sb content by the intensity ratio of XRD peaks corresponding to (009) and (0015) planes. The peaks corresponding to (009) and (0012) are absent in Bi_2Te_3 but present in Sb_2Te_3, due to diffraction form factor. Hence, intensity ratio of (009) to (0015) is feasible to determine Sb content with the help of XRD. In present sample, intensity (area under the peak) ratio is $I_{(009)}/I_{(0015)}$ ~0.067, suggesting approximately 50% of Sb content [104]. We have also performed the powder XRD of $BiSbTe_3$ sample after grinding the single crystal sample. To determine lattice parameters, we have analyzed powder XRD data by Le Bail refinement using the Full Prof software (figure 4.1 (b)). All peak positions of $BiSbTe_3$ sample corresponding to the standard Bragg positions of rhombohedral crystal structure belonging to the space group D_{3d}^5 ($R\bar{3}m$) have been shown by the vertical bars and the residue by the line respectively at the bottom of the XRD patterns. The calculated lattice parameters are $a = b$ = 4.32(4) Å, c = 30.48(2) Å and cell volume is 493.54(4) $Å^3$, whereas the calculated α, β and γ values are 90˚, 90˚ and 120˚. All the extracted values from Le Bail refinement of XRD spectra are matched with the reported values [105]–[107]. Le Bail analysis indicates that the sample is single phase and no trace of other impurities has been found. The impurities can be detected by XRD only when they form crystalline phases. Hence there is no crystalline impurity within the detection limit of XRD.

In order to see the pressure dependency on the structure of the investigated system we have performed XRD experiment with pressure variation using diamond anvil cells.

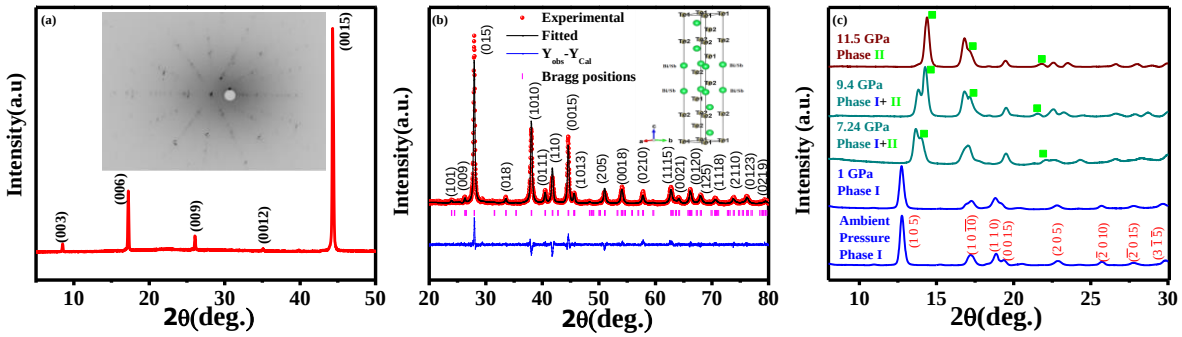

Figure 4.1: (a) Single crystal X-ray diffraction of $BiSbTe_3$ cleaved along (*00l*) direction, Inset: Laue diffraction pattern (b) Le Bail refinement of powder XRD of as grown $BiSbTe_3$ single crystal sample using Full Prof software. (c) X-ray diffraction-patterns of $BiSbTe_3$ at various pressures with wavelength 0.7101 Å. The peaks indicated with solid Green Square are the reflections from high pressure phase.

Figure 4.1 (c) illustrates the diffraction pattern of $BiSbTe_3$ polycrystalline sample (ground from single crystal sample) under various pressures at room temperature. It is clear from figure 4.1 (c) that evaluation of secondary phase is started from 7.24 GPa and persisted up to 11.5 GPa. But at 11.5 GP monoclinic phase (secondary Phase) is dominating over rhombohedral phase which is consistent with reported results [98], [108], [109]. Therefore, rhombohedral $R\bar{3}m$ phase is robust below 11.5 GP as observed from pressure XRD as well as from theoretical calculation (discussed below).

Furthermore, to specify the elements in the system, we have performed XPD for $BiSbTe_3$ sample on (111) surface. We have used photon energy 416 eV for Bi *4f* and 300 eV for Sb *4d* and Te *4d* core levels. XPD patterns recorded for emitter core level as photoemission peak intensity. The XPD patterns give the information of the atomic structure, which enable a direct reconstruction of the local environment around certain atom. It is confirmed from the XPD that all three elements are present in the sample. X-ray photoelectron holography of Sb, Bi and Te core level are shown in figure 4.2.

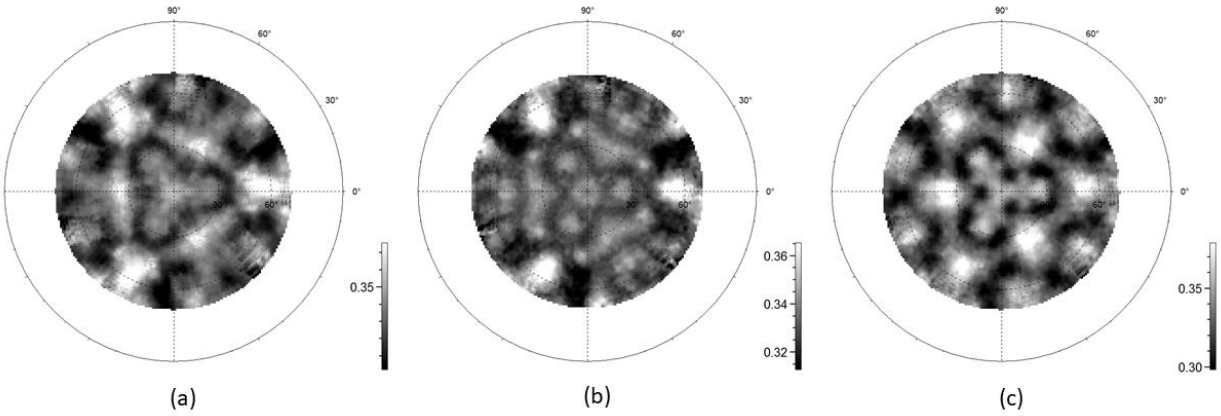

Figure 4.2: Experimental photoelectron diffraction patterns obtained for the Bi *4f* (a), Sb *4d* (b) and Te *4d* (c) from the (1 1 1) surface of $BiSbTe_3$.

Figure 4.3 (a) shows the variation of the electrical resistance (R) at various pressures, where R is decreased when pressure is increased from 2 GPa to 6 GPa. However, no sharp transition in the resistance was observed up to the lowest measured temperature (~2 K) (inset: figure 4.3 (a)). When pressure was further increased to 8 GPa, a sharp decrease in resistance is observed with T_{onset} = 2.47 K. At pressure 8.25 GPa, a similar transition occurred at a little higher onset temperature (T_{onset} = 2.51 K). This sharp decrease in the resistance at a particular temperature above 8 GPa can be assigned as the superconducting transition. The superconducting transition is enhanced with increasing pressure and T_{onset} also shifts towards higher value as shown in the inset of figure 4.3 (b). The highest T_{onset} (3.36 K) was observed at 14 GPa, above which it becomes almost constant up to 15 GPa. Inset of figure 4.3 (b) displayed that above 11 GPa pressure, resistance value dropped to zero before reaching 2 K and simultaneously transition becomes sharper. The phase diagram of T_C^{zero} (at which resistance dropped to zero) and T_{onset} with pressure is shown in figure 4.3 (b).

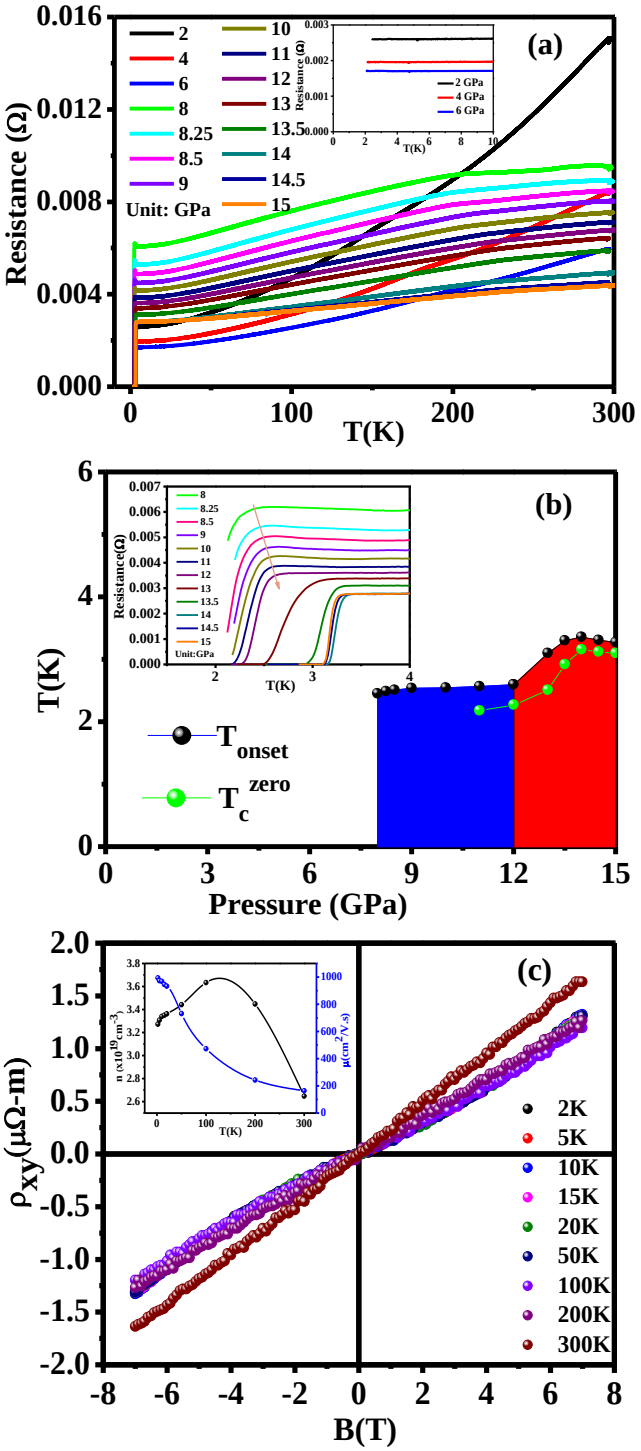

Figure 4.3: (a) Temperature dependent of resistance at different pressures with a superconducting transition around 8 GPa. Inset: Variation of resistance with respect to temperature at 2, 4 and 6 GPa (b) Variation of superconducting transition temperature with respect to applied pressure of $BiSbTe_3$. Inset: Close view of temperature dependent resistance at different pressures. (c) Magnetic field dependence of the Hall resistivity at different temperatures. Inset: variation of carrier density and mobility as a function of temperature.

Figure 4.3 (c) shows the variation of Hall resistivity (ρ_{xy}) with the magnetic field (B) at different temperatures. The Hall resistivity is linear with positive slope indicating the *p*-type nature of the sample. The slope of Hall data increases above 100 K suggesting the increase in the carrier concentration (*n*). The carrier concentration obtained from Hall data is ranging from 3.63 $\times 10^{19} cm^{-3}$ (2 K) to 2.64×10^{19} cm^{-3} (300 K) and the obtained Hall mobility is ranging from 993 $cm^2/V.s$ (2 K) to 164 $cm^2/V.s$ (300 K) (Inset: figure 4.3 (c)) [94], [106], [110]. The increase in carrier concentration above 100 K might be due to the increase of bulk contribution. However, the decrease of mobility with increase of temperature is due to the enhancement of thermal vibration.

Figure 4.4 (a) and 4.4 (c) represent the ARPES spectra taken at 20 K and 60 K, respectively. These images show the BVB of the $BiSbTe_3$ forming a V-shaped valley like bulk band gap region around the Γ-point in the Brilliouin zone and the topological surface state (TSS) residing inside it as observed earlier [92]–[94]. The sharpness of the linear dispersion of the TSS reveals good quality of the sample as well as the high energy and momentum resolution of the laser ARPES spectra. Note that one can discern the unoccupied part of the Dirac cone (DC) related to the TSS above E_F at 60 K due to the thermal broadening of the Fermi distribution function. The DP is seen to lie near E_F in this compound which happens to be an ideal condition for the technological exploitation of the topological properties of the TSS. We have fitted the momentum distribution curves (MDCs) peak position using two Voigt function in the range of -30 to -5 meV. We have fitted the straight line and with the fitting results we found that the DP lies at the E_F with the error of ±2 meV. The fitting of MDCs plots offers clarity in visualizing the DP. This is

important because the parent compounds Bi_2Te_3 and Sb_2Te_3 are mainly of *n*-type and *p*-type [28], [90]–[94].

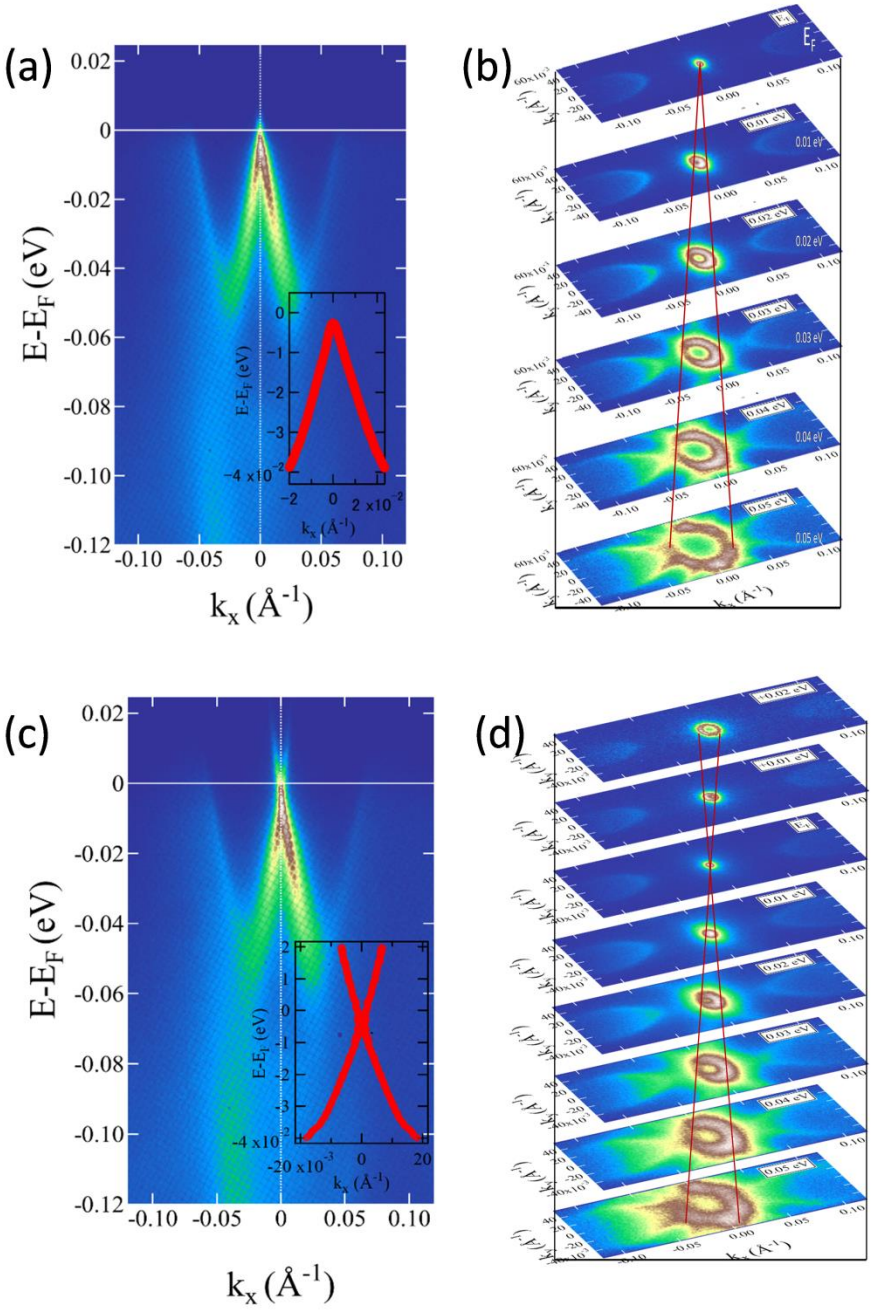

Figure 4.4: Band structure of the $BiSbTe_3$ single crystal measured at T=20 K ((a) and (b)) and 60 K ((c) and (d)). Inset of figure (a): the EDC curve fitting. (b) The stacked plots of the iso-energy contours of the ARPES spectra at T=20 K. Inset of figure (c): the MDC curve fitting. (d) The stacked plots of the iso-energy contours of the ARPES spectra at T=60 K.

Doping Sb for Bi is expected to tune the DP at E_F for some of the intermediate composition. Accordingly, when we doped Sb in place of Bi halfway, we could realize a rare and important feat of tuning the DP to E_F. Thus the surface of this particular compound could potentially prove to be useful in realizing the promises of the TSS for practical applications. Surprisingly, the transport properties for this compound show a *p*-type behavior which is difficult to be understood entirely from the states near DP. From ARPES spectra we observe a finite contribution from the BVB towards E_F which is due to its specific band dispersion enclosing a valley type of bulk band gap containing the DP. Thus when E_F is at the DP the surrounding peaks from the BVB simultaneously also cross E_F giving rise to a net *p*-type electrical transport in this compound since the states of the BVB have a *p*-type dispersion.

Figure 4.4 (b) and 4.4 (d) depict the iso-energy contours of the ARPES spectra respectively at 20 K and 60 K. Here we are able to see the sharpness of DP at 20 K and the emergence of the unoccupied part of the DC at 60 K clearly. The vertically stacked iso-energy contours taken at different binding energies (BEs) clearly reveal the 3D view of the DC around the Γ-point. The bright circular central contour surrounding the Γ-point arises from the TSS while the BVB reveals a six-fold petal like structure around the central contour. At higher BE the central contour touches the petal structure. Upon approaching E_F it shrinks while the petal structure expands which is consistent with the band dispersion of the respective states. Here again we observe a point like Fermi surface (FS) arising due to the DP in concurrence with the occurrence of the DP at E_F. At higher BE the DC is seen to develop slight warping. Such a warping in the FS is known to originate from the effect of spin orbit coupling in the electronic structure of topological insulators [6], [111].

4.3.2 Theoretical study

Furthermore, to understand the electronic structure of the system we have also performed the density functional theory (DFT) study using the Vienna ab initio simulation package (VASP) under the generalized gradient approximation (GGA). A rhombohedral structure with $R\bar{3}m$ space group is used, and these calculations are performed with K-mesh of 6x6x1. We have considered a plane-wave basis up to cut-off energy 600 eV for convergence with force convergence below 0.001 eV $(Å)^{-1}$. The spin-orbit coupling value is chosen to default value in VASP package for Bi atoms. The surface calculations are done using 6 quintuplets and with vacuum layer of 20 Å to avoid interactions between adjacent slabs for the (111) surface.

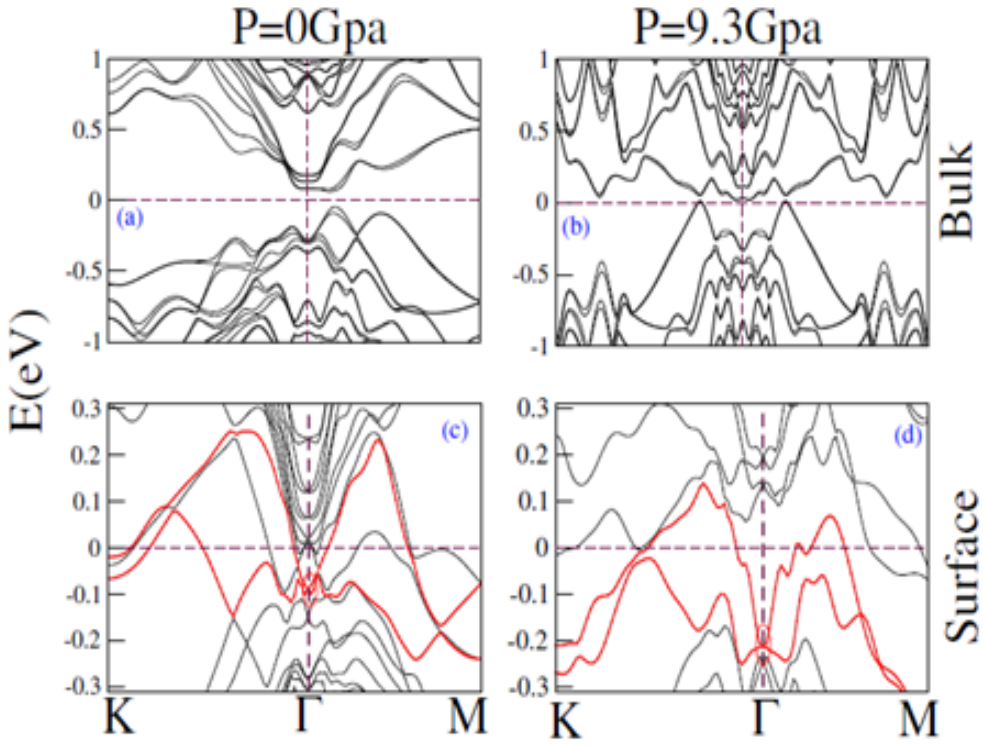

Figure 4.5: Electron dispersion E curve of $BiSbTe_3$ Bulk systems are shown for P=0 and 9.3 Gpa in (a) and (b), whereas, in (c) and (d) electronic dispersions E are shown for 6 quintuple layers at 0 and 9.3 Gpa. Red curve represents the surface states which forms the Dirac points and the Dirac point encircle in the circle at the Γ-point.

To understand the effect of the hydrostatic pressure P on band structure of $BiSbTe_3$, we calculate electronic structure for various values of P. We notice that, in bulk, p-orbital band of Te moves up and crosses the Fermi-surface at P=8.5 GPa in absence of the spin-orbit coupling, and however the crossing occurs at P ~9.3 GPa as shown in panel (b) of figure 4.5. With increasing pressure other conduction bands move down near the Fermi-energy level. The surface states are shown in the panel (d) of figure 4.5. Orbitals of all three atoms Bi, Sb and Te crossed the Fermi-surface, whereas the bands near Γ-point are either from Te or Sb. Interestingly, the Dirac point is still intact and moves away from Fermi-surface. Therefore, in the origin of superconductivity in this material there exists multi-orbital contribution. For P > 11 GPa the $BiSbTe_3$ have finite DOS at Fermi-energy. Furthermore, the theoretical calculation suggests that with pressure surface states remains topologically protected and only change is observed in the bulk band structure.

4.4 Conclusion

We have investigated the external pressure effect on the resistance, and the ARPES on $BiSbTe_3$. X-ray photoelectron diffraction shows that Bi, Sb and Te elements present in the sample. It is observed that with increase of pressure resistance decreases and at a value of 8 GPa a sharp drop in resistance is observed which indicates the occurrence of superconductivity. With further increase of pressure, the superconducting transition temperature (T_c) increases and at 14 GPa it shows the maximum T_c (~3.3 K). This may indicate that the superconducting transition might be due to the change in the bulk band structure in $BiSbTe_3$. Furthermore, the ARPES study clearly indicates the Dirac point is located at the Fermi level. Theoretical study indicates that surface states remain

topologically protected and bulk band structure changes under applied pressure. This is an ideal condition for the technological exploitation of the topological properties of the TSS.